ACS APPLIED MATERIALS & INTERFACES

Research Article

www.acsami.org

Manganese Doped Iron Oxide Theranostic Nanoparticles for Combined T_1 Magnetic Resonance Imaging and Photothermal Therapy

Mengxin Zhang,[†,∥] Yuhua Cao,[†,‡] Lina Wang,[†,§] Yufei Ma,[†] Xiaolong Tu,[†] and Zhijun Zhang*[,†]

[†]Key Laboratory for Nano-Bio Interface, Division of Nanobiomedicine, Suzhou Institute of Nano-Tech and Nano-Bionics, Chinese Academy of Sciences, Suzhou 215123, China

[‡]College of Life and Health Sciences, Northeastern University, NO. 3-11 Wenhua Road, Shenyang 110819, China

[§]School of Life Sciences, Shanghai University, 99 Shangda Road, Shanghai 200444, China

[∥]University of Chinese Academy of Sciences, 19 Yuquan Road, Beijing 100049, China

Supporting Information

ABSTRACT: Photothermal therapy (PTT) is a noninvasive and convenient way to ablate tumor tissues. Integrating PTT with imaging technique could precisely identify the location and the size of tumor regions, thereby significantly improving the therapeutic efficacy. Magnetic resonance imaging (MRI) is widely used in clinical diagnosis due to its superb spatial resolution and real-time monitoring feature. In our work, we developed a theranostic nanoplatform based on manganese doped iron oxide (MnIO) nanoparticles modified with denatured bovine serum albumin (MnIO-dBSA). The in vitro experiment revealed that the MnIO nanoparticles exhibited T_1-weighted MRI capability (r_1 = 8.24 mM^{-1} s^{-1}, r_2/r_1 = 2.18) and good photothermal effect under near-infrared laser irradiation (808 nm). Using 4T1 tumor-bearing mice as an animal model, we further demonstrated that the MnIO-dBSA composites could significantly increase T_1 MRI signal intensity at the tumor site (about two times) and effectively ablate tumor tissues with photoirradiation. Taken together, this work demonstrates the great potential of the MnIO nanoparticles as an ideal theranostic platform for efficient tumor MR imaging and photothermal therapy.

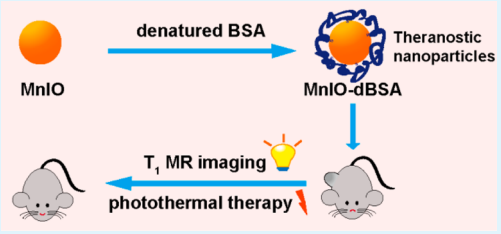

KEYWORDS: *magnetic nanoparticles, MR imaging, photothermal therapy, theranostics*

INTRODUCTION

Photothermal therapy (PTT) is a form of medical treatment of disease, especially cancer by using the light-induced temperature rise. With this hyperthermia effect, cancer cells can be killed due to the denaturation of proteins and the disruption of cell membranes in the diseased sites at higher temperature.[1] PTT has distinct advantages over chemotherapy and radiotherapy, due to its noninvasiveness, low side effect, and convenience, and therefore is considered as a very useful alternative strategy for solid tumor treatment.[2] Compared with visible light, using near-infrared (NIR) light from 700 to 1400 nm, also called biological windows, can reduce the strong absorption of human tissues and allow deep tissue penetration.[3] In recent years, a variety of nanomaterials which are capable of generating efficient heat under NIR laser irradiation have been studied intensively. These nanomaterials include gold nanostructured materials,[4,5] copper sulfide,[6] molybdenum sulfide,[7,8] and carbon materials such as carbon nanotube,[9,10] carbon dots,[11,12] and graphene.[13,14] Applying PTT agents into the tumor site could increase treatment efficiency and meanwhile minimize the damage to the surrounding healthy tissues.[3] In order to precisely identify the location and size of the tumor region, the combination of imaging modality with therapy is usually adopted for optimal medical outcome.[15]

Magnetic resonance imaging (MRI) is a widely used clinical diagnosis technique with high spatial resolution and real-time monitoring.[16] In order to accurately distinguish lesion site from normal tissues, MRI contrast agents (CAs) are commonly employed to improve the contrast between the pathological and normal areas. There are two types of MRI CAs: the T_1 and T_2 CAs.[17] Most of T_1 CAs are gadolinium based complexes. Gadolinium species improve T_1 relaxation time by changing the interactions between water protons and electron spins of CAs, leading to a brighter image.[18] T_2 CAs used in clinical diagnosis mainly refer to superparamagnetic iron oxide nanoparticles (SPIONs) with a size smaller than 20 nm.[19] Under external magnetic field, the secondary magnetic field produced by SPIONs, can induce a faster T_2 relaxation time of water protons, resulting in a darker image.[20] However, because T_2 MR images can be confused with hypointense lesions and the "blooming effect" generated by SPIONs, positive T_1 contrast

Received: November 17, 2014
Accepted: February 12, 2015
Published: February 12, 2015

DOI: 10.1021/am5080453
ACS Appl. Mater. Interfaces 2015, 7, 4650−4658

effect is preferred in some clinical diagnosis.[21] Due to the toxicity of gadolinium complexes, especially to patients with kidney disorders, many efforts have been devoted to develop nongadolinium CAs in recent years.[22] One of the appealing strategies is to fabricate small-sized magnetic iron oxide nanoparticles. Since MR imaging effect of magnetic nanoparticles is strongly related to their size, large-sized iron oxide nanoparticles have strong T_2-weighted MR effect because of their high magnetic moment.[23] When reducing the size of iron oxide nanoparticles, their magnetic moment decreases rapidly due to reduction in the volume magnetic anisotropy and the pronounced surface spin canting effect.[18,24] As a result, small-sized iron oxide nanoparticles become T_1 CAs due to the attenuated T_2 effect. Besides reducing the size of iron oxide nanoparticles, doping metal iron, such as Gd^{3+}, Mn^{2+}, Zn^{2+}, and Ni^{2+}, into iron oxide is another effective strategy to increase the T_1 signal.[25−27] Gao and co-workers embedded gadolinium into iron oxide (GdIO) and demonstrated that the 4.8 nm GdIO nanoparticles have significantly enhanced T_1 MRI effect.[25] By adopting one-step high-temperature coprecipitation method, Li et al. synthesized ultrasmall manganese ferrites ($MnFe_2O_4$) nanoparticles with a diameter of 2.2 nm, which also exhibited pronounced T_1 contrast.[26] The enhanced T_1 positive effect may attribute to the large unpaired electrons of paramagnetic Gd^{3+} and Mn^{2+} iron. Moreover, the embedded gadolinium species disturbed the long-range order of magnetic spins in iron oxide nanoparticles. Considering the potential renal toxicity of gadolinium complexes, it is desired to develop small-sized iron oxide nanoparticles with manganese dopping for T_1 enhanced imaging.

In this work, we have developed manganese doped iron oxide (MnIO) theranostic nanoparticles with a desired size for cancer T_1 imaging and photothermal therapy. To the best of our knowledge, there is no report on the combined T_1 MR imaging and photothermal theranostic system based on magnetic iron oxide nanoparticles. The MnIO nanoparticles were synthesized by hydrothermal method. To improve the biocompatibility of the MnIO nanoparticles, we employed a biomolecule, denatured bovine serum albumin (dBSA), to modify the surface of MnIO nanoparticles. We further demonstrated that thus-prepared MnIO-dBSA composites exhibited excellent T_1 MR imaging and photothermal effect both in vitro and in vivo. The synthesis route and MRI and photothermal experiment is shown in Scheme 1.

Scheme 1. Illustration of Preparation of MnIO-dBSA Composites and Combined in Vivo T_1 MR Imaging and Photothermal Effect

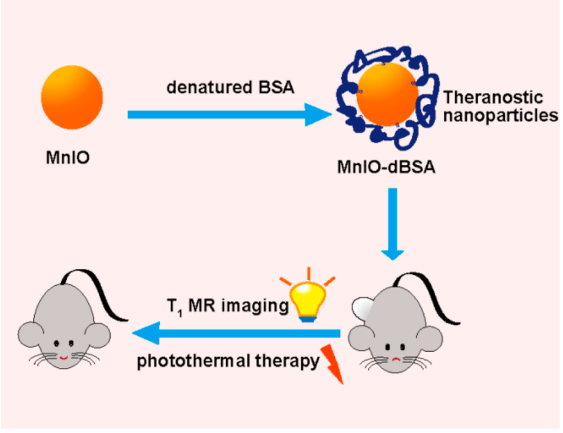

EXPERIMENTAL SECTION

Materials. Diethylene glycol and bovine serum albumin (BSA) were purchased from Sigma-Aldrich and Sangon Biotech, respectively. WST-1 was purchased from Beyotime Biotechnology Institute. All other reagents were purchased from China National Medicine Corporation. All the chemicals and materials were used as received without further purification. Ultrapure water (18.2 MΩ·cm) was used throughout the experiments.

Instruments. MnIO nanoparticles were characterized with a Tecnai G2 F20 S-Twin transmission electron microscope (TEM) at an accelerating voltage of 200 kV. X-ray diffraction (XRD) analysis was conducted by a Bruker D8 Advance X-ray diffractometer (with Cu Ka radiation at 0.15418 nm). Fourier transform infrared (FT-IR) spectra were collected using a Thermo Nicolet 6700 FTIR spectrometer. UV−vis−NIR spectra were obtained with a PerkinElmer Lambda 750 spectrophotometer. Hysteresis loop was recorded on a Quantum Design physical property measurement system (PPMS-9T, EC-II) at 300 K. Thermogravimetric analysis was performed on a SII-EXSTAR 6000 TG/DTA 6200 thermobalance. Fluorescence microscope images were captured on a Nikon A 1R laser confocal microscope. Dynamic light scattering (DLS) was determined by a particle size/zeta analyzer (ZEN3600-nanoZS, Malvern). MRI measurements were performed on a Micro MR Analyzing system (PQ001, Shanghai Niumag Corporation) with magnetic field of 0.5 T. Cell lines were maintained in a humid CO_2 incubator (Thermo 3111). WST-1 assay was read out from a PerkinElmer 2030 multilabel reader. Infrared (IR) thermal images were taken by IR thermal camera (FLIR SC325, USA). The concentration of Fe or Mn in all samples was determined by an inductively coupled plasma optical emission spectrometer (ICP-OES, Thermo scientific iCAP 6200).

Synthesis of MnIO Nanoparticles. The synthesis procedure of MnIO nanoparticles was modified with literature.[28] In a typical synthesis of MnIO nanoparticles, iron(III) chloride hexahydrate ($FeCl_3·6H_2O$, 0.1802 g) and manganese(II) chloride tetrahydrate ($MnCl_2·4H_2O$, 0.0659 g) were mixed with 10 mL of diethylene glycol and heated to 80 °C under vigorous agitation. Then, trisodium citrate dihydrate ($Na_3Cit·2H_2O$, 0.1176 g) was added and stirred for 1 h to form a clear solution. Following that, anhydrous sodium acetate (CH_3COONa, 0.2461 g) was added. After stirring for 30 min, the above solution was transferred into a 20 mL Teflon-lined stainless-steel autoclave. The autoclave was then heated and kept at 200 °C for 6 h. When the autoclave was cooled to room temperature, the product was washed with ethanol and collected with a magnet, and the procedure was then repeated for three times. After that, the product was dispersed in 15 mL of water and dialyzed for 2 days to remove impurities. The synthesis of iron oxide with similar size as MnIO nanoparticles was carried out under the same condition, and the initial iron(III) chloride hexahydrate was 0.2703 g.

Preparation of MnIO-dBSA Composites. MnIO-dBSA composites were synthesized following a modified literature procedure.[29] In brief, 0.165 g of BSA was dissolved in 50 mL of water and then 0.0042 g of $NaBH_4$ was added into the solution. After stirring at room temperature for 1 h, the solution was heated to 70 °C for another 1 h. Following that, 10 mL of MnIO nanoparticles was added into 20 mL of dBSA solution and stirring at 70 °C for 2 h. When cooled to room temperature, the solution was collected and rinsed with water through spin-dialysis (100 kDa cutoff, 5000 rpm) to remove the impurities. The 100 kDa cutoff spin column was also used to concentrate the solution of MnIO-dBSA composites.

In the agarose gel electrophoretic experiment, 10 μL of MnIO nanoparticles solution and 10 μL of MnIO-dBSA composites solution were mixed with 10 μL of sample buffer, respectively, and then loaded into the well of the 0.8% agarose gel which was immersed in the TAE running buffer for electrophoretic analysis. The agarose gel was stained with Coomassie blue for protein detection when the Bromophenol blue in the sample buffer run to the middle of the gel.

Cell Culture. HeLa cells and murine breast cancer cell line 4T1 were purchased from Shanghai Institutes for Biological Sciences,

DOI: 10.1021/am5080453
ACS Appl. Mater. Interfaces 2015, 7, 4650−4658

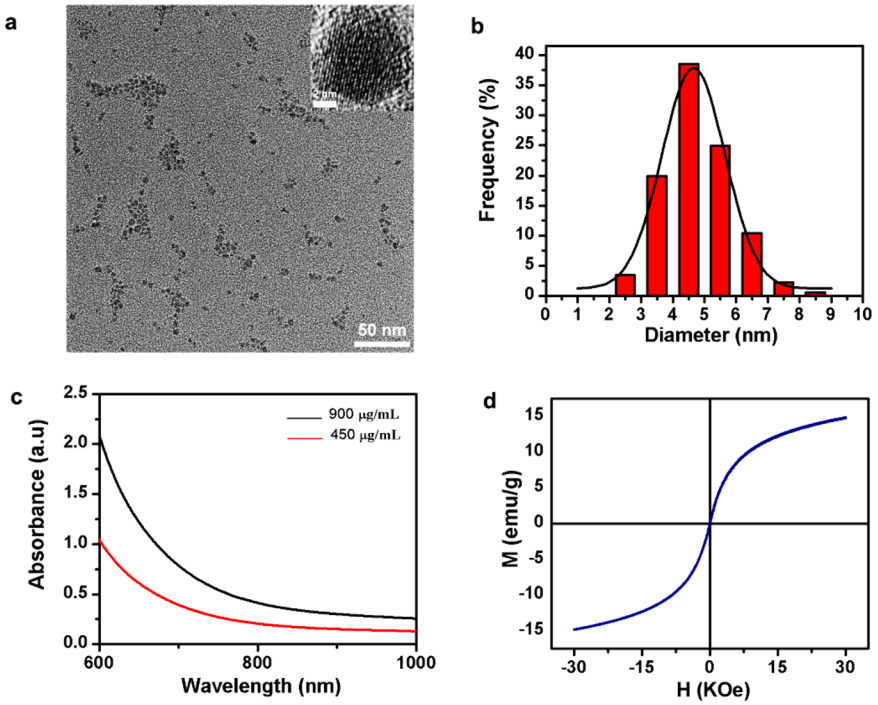

Figure 1. (a) TEM and HR-TEM (insert) images of MnIO nanoparticles, the scale bar is 50 and 2 nm, respectively. (b) Size distribution analysis of MnIO nanoparticles by TEM (n = 300). (c) UV−vis−NIR spectra of MnIO nanoparticles in aqueous solution at different Fe concentrations. (d) Magnetization curve of MnIO nanoparticles at 300 K.

Chinese Academy of Sciences. The two cancer cells were cultured in RPMI-1640 cell medium containing 10% fetal bovine serum (FBS, Hyclone), streptomycin at 100 μg/mL, and penicillin at 100 units/mL, respectively, and maintained at 37 °C in a humidified atmosphere of 5% CO_2 in air.

Cytotoxicity Assessment. Cytotoxicity of MnIO-dBSA composites was evaluated using WST-1 assay. HeLa or 4T1 cells were seeded into 96-well plates at a density of 8×10^3 cells/well and maintained for 24 h. Then the aqueous solution of the MnIO-dBSA composites at various concentrations were added into 96-well plates and incubated for another 24 h. Relative cell viability was then evaluated by standard WST-1 assay.

Tumor Model. Healthy female BALB/c mice at an average age of 6−7 weeks (18−22 g) were purchased from Suzhou Industrial Park Animal Technology Co., Ltd. All animal experiments were performed under the protocols approved by Soochow University Laboratory Animal Center. 4T1 tumor-bearing mice were prepared by subcutaneous injection of 2×10^6 4T1 cells (in 50 μL of serum free cell culture medium) at the right hind leg of the female BALB/c mice. When the average tumor size reached 120 mm^3, the mice were used for experiments.

MRI Measurements. To obtain T_1 relaxation times of the aqueous solution of the MnIO nanoparticles at different concentrations, following measurement parameters were used: repetition time (TR) = 6000 ms, number of data =25, and number of averages (NA) = 2. While the T_2 relaxation times were determined with the following parameters: TR = 6000 ms, echo time (TE) = 1 ms, echo count = 6000 and NA = 2. Both r_1 and r_2 relaxivities were calculated by the linear fitting of $1/T_1$ or $1/T_2$ as a function of metal (Fe + Mn) concentration. For T_1-weighted MR images, the instrument parameters were set as follows: TR = 100 ms, TE = 18.2 ms, imaging matrix = 192 × 256, slice thickness = 5 mm, field of view (FOV) = 100 mm × 100 mm and NA = 2.

For in vivo T_1 MR imaging experiments, the MR images were obtained at a 0.55 T MRI scanner (MesoMR60, Shanghai Niumag Corporation). A tumor-bearing mouse was anesthetized with 100 μL of 10% chloral hydrate through intraperitoneal injection. 200 μL of MnIO-dBSA solution was injected intravenously into the mouse ([Fe] = 14 mg/kg). MR images were acquired before injection and at 0.5, 1, 4, 6, and 12 h postinjection (p.i.), respectively. To further quantify signal enhancement of the tumor site in T_1 MR images, the following equation was used:[30]

$$\text{signal enhancement} = (R_{\text{p.i.}} - R_0)/R_0$$

where R_0 and $R_{\text{p.i.}}$ were defined as signal-to-background ratios before and after injection of MnIO-dBSA solution.

All the images were acquired using multiple spin echo sequence under the following parameters: TR = 300 ms, TE = 18.2 ms, imaging matrix = 192 × 256, slice thickness = 3.0 mm, slice gap = 0.6 mm, FOV = 80 mm × 80 mm and NA = 8.

Photothermal Effect. To evaluate the photothermal effect of the MnIO nanoparticles, 200 μL of aqueous solution of the MnIO nanoparticles with different concentrations was added into a 1.5 mL vial and irradiated under an NIR laser (808 nm, 2 W) for 5 min. A detection probe was inserted into the aqueous solution, and a digital thermometer was used to record the temperature during the irradiation. The thermocouple probe should be mounted carefully to avoid direct laser irradiation. The photothermal conversion efficiency was calculated according to the literature.[31] In brief, 500 μL of MnIO nanoparticles solution (Fe: 500 μg/mL) was irradiated by the 808 nm laser (2 W). When the temperature of the solution reached a steady state, the laser was turn off and allowed the solution to cool naturally. The temperature was recorded every 30 s during the process.

In Vitro Photothermal Treatment of the Cancer Cells. 4T1 cells were seeded into 96-well plates at a density of 1×10^4 cells per well. After incubation for 24 h, aqueous solution of MnIO-dBSA composites with different concentrations was added and then exposed to an NIR laser (808 nm, 2 W) for 5 min. The cell viability was measured using standard WST-1 assay after laser irradiation. For calcein acetoxymethyl ester (calcein-AM) and propidium iodide (PI) costaining, 2×10^4 4T1 cells were seeded into 48-well plates for 24 h. Then the photothermal treatment was conducted as above. After washed twice with PBS, the cells were incubated with a mixture of calcein-AM and PI solution for 20 min. Following that, a confocal fluorescence microscope was employed to capture the fluorescence images.

DOI: 10.1021/am5080453
ACS Appl. Mater. Interfaces 2015, 7, 4650−4658

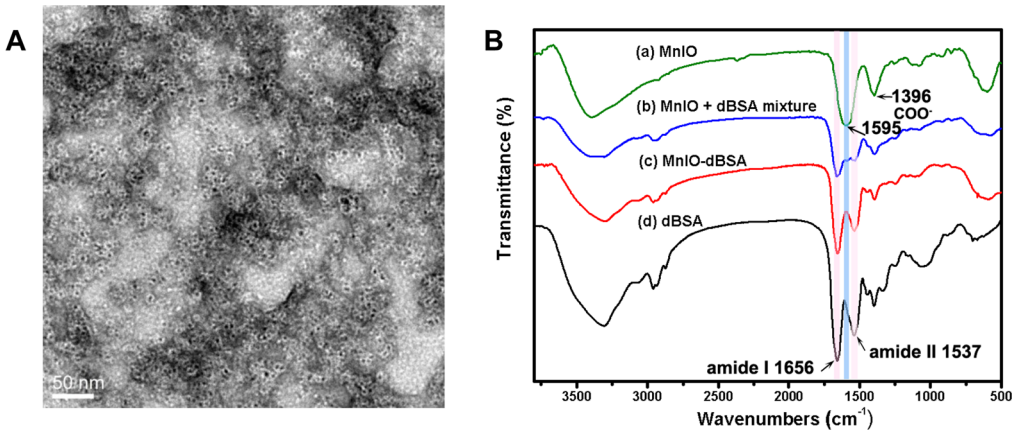

Figure 2. (A) TEM image of MnIO-dBSA composites stained with 2% tungstophosphoric acid. (B) FT-IR spectra of (a) MnIO nanoparticles, (b) MnIO + dBSA mixture, (c) MnIO-dBSA composites, and (d) dBSA.

In Vivo Photothermal Therapy. The 4T1 tumor-bearing mice were randomly divided into four groups with four mice in each group. When the average size of the tumor reached 120 mm^3, the mice were anaesthetized with 100 μL of 10% chloral hydrate and used for photothermal therapy. For PBS + laser and MnIO-dBSA + laser groups, the mice were given 100 μL of PBS or MnIO-dBSA solution ([Fe] = 40 mg/kg) through intratumoral injection, respectively. After 20 min, the mice were irradiated with an NIR laser (808 nm, 1.5 W) for 5 min. An IR thermal camera was used to monitor the temperature change of the tumor site. For PBS − laser and MnIO-dBSA − laser groups, the mice were only injected with 100 μL of PBS or MnIO-dBSA, respectively, but without laser irradiation. In the following 19 days, the size of the tumor and the weight of the mice were monitored every the other day to evaluate the therapeutic efficacy. The tumor size was measured by a caliper and calculated as tumor size = (tumor length) × (tumor width)^2/2. Relative tumor volumes were calculated as V/V_0, where V_0 was the tumor volume at initial time of treatment.

Blood Biochemical Analysis and Histopathological Assessment. Blood biochemical analysis was conducted following a standard protocol. Three mice of the MnIO-dBSA + laser group were sacrificed on the 19th day after irradiation treatment. Blood serum was then collected to examine the influence of MnIO-dBSA on liver and kidney functions. Three untreated healthy and age-matched BALB/c female mice were chosen as a control group. For histopathological assessment, organs (heart, liver, spleen, kidney, and lung) of the mice from MnIO-dBSA + laser and control group were harvested and fixed in 10% formalin solution. After H&E staining, the slices were observed using an optical microscope.

Statistical Analysis. Data of the cell and animal experiments were presented as mean ± standard deviation. One-tailed Student's test was applied to evaluate the significance among groups, and $p < 0.05$ was considered to be statistically significant.

RESULTS AND DISCUSSION

Synthesis of MnIO Nanoparticles. The MnIO nanoparticles were synthesized by the hydrothermal method. Thus-prepared nanoparticles are well-dispersed in aqueous solution. TEM results indicated that these nanoparticles were uniform (Figure 1a). As shown in the size distribution profile, the size of the MnIO nanoparticles is about 3−6 nm, with the average diameter of 5.0 nm (Figure 1b, n = 300), which is desirable as a T_1-weighted MRI CAs.[26,32,33] The DLS measures further releaved the narrow size distritubion of MnIO nanoparticles (Supporting Information (SI), Figure S1). The prepared MnIO were aslo chracterized with XRD and EDAX (SI, Figures S2 and S3). The XRD pattern exhibited the spinel sturcture of the MnIO nanoparticles. The molar ratio of Fe/Mn was determined to be 1:0.28 by ICP-OES. UV−vis−NIR spectra of MnIO nanoparticles revealed a broad absorption from ultraviolet to near-infrared range, and the absorbance is concentration-dependent (Figure 1c). From the saturation magnetization curve obtained by the field-dependent magnetization measurement at 300 K, the saturation magnetization value (M_s) was determined to be 15.0 emug/g, and the absence of a hysteresis hoop indicated the superparamagnetic property of the MnIO nanoparticles (Figure 1d).

Preparation of MnIO-dBSA Composites. To improve the biocompatibility, the MnIO nanoparticles were modified with denatured BSA. In the presence of reductive agent $NaBH_4$, disulfide bridges of BSA are converted to sulfhydryl groups, resulting in the chemical denaturation of the protein. Denatured BSA is considered as a biomacromolecule containing 34 thiol groups per monomer. It was employed to cap quantum dots to improve chemical stability and photoluminescence quantum yield.[34] The TEM image of MnIO-dBSA composites showed a thin layer of dBSA modified on the surface of the MnIO nanoparticles (Figure 2a). The DLS analysis further verified the monodispersity of MnIO-dBSA composites (Figure S4). In Figure 2b, the FT-IR spectrum of MnIO nanoparticles exhibited the characteristic peaks of the carboxylate group at 1595 and 1396 cm^{-1}, attributed to citrate groups capping on the surface of the MnIO nanoparticles. The dBSA spectrum showed the amide I and amide II bands located at 1656 and 1537 cm^{-1}, respectively. When simply mixed MnIO nanoparticles and dBSA together, the characteristic peaks coming from the two samples were detected. In contrast, for MnIO-dBSA composites, only the dBSA signal was observed, suggesting that the surfaces of the MnIO nanoparticles have almost been replaced by dBSA molecules. In electrophoretic analysis, the brown color was observed in both MnIO and MnIO-BSA bands, but only MnIO-BSA exhibited blue color after staining with Coomassied blue (SI, Figure S5a), indicating the presence of the protein. Thermogravimetric analysis (TGA) showed about 20% weight loss of MnIO-dBSA compared with MnIO nanoparticles (SI, Figure S5b). These experiments together verify the successful modification of dBSA onto the MnIO nanoparticles. Moreover, the amino and carboxyl groups remaining on dBSA provide reactive sites for further functionalization.[35,36] The MnIO-dBSA composites were stable in physiological solutions, with no obvious aggregations observed in both cell culture medium and PBS over 5 days (SI, Figure S6).

DOI: 10.1021/am5080453
ACS Appl. Mater. Interfaces 2015, 7, 4650−4658

The low toxicity of the nanomaterials is a prerequisite for their biomedical applications. The in vitro toxicity of the MnIO-dBSA composites was evaluated. After HeLa and 4T1 cells were incubated with MnIO-dBSA for 24 h, the relative cell viability was about 80% up to 200 μg/mL, suggesting the low cytotoxicity of the MnIO-dBSA composites (SI, Figure S7).

In Vitro MRI. To investigate the contrast enhancement of the MnIO nanoparticles, longitudinal relaxivity r_1 and transverse relaxivity r_2 of MnIO nanoparticles were calculated from the linear fitting of $1/T_1$ or $1/T_2$ plot versus metal concentrations (Figure 3a). The values of r_1 and r_2 are

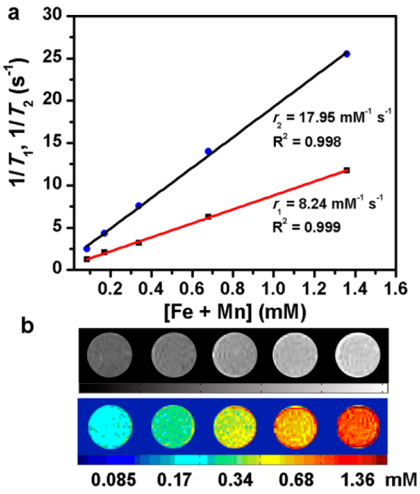

Figure 3. (a) Plots of $1/T_1$ and $1/T_2$ as a function of total metal (Fe + Mn) concentrations. (b) T_1-weighted MR images (top) and their color-coded images (bottom) of the MnIO aqueous solution at various metal concentrations (Fe + Mn).

estimated to be 8.24 and 17.95 mM^{-1} s^{-1}, respectively. More importantly, the ratio of r_2/r_1 is calculated to be 2.18, and the low ratio of r_2/r_1 indicates that the MnIO nanoparticles can be used as T_1 MRI CAs.[28,33] As shown in Figure 3b, the MnIO nanoparticles present excellent positive T_1 contrast enhancement, and the brightness of MR images enhances with the increasing concentration of MnIO solutions, showing a clear dose-dependent color change, due to the relaxation of water proton increases with the increase of concentration dose.[37] In order to improve T_1 positive contrast effect, iron oxide nanoparticles with a smaller size are usually synthesized to suppress their negative effect.[18,23] Doping of Mn (II) into the iron oxide nanoparticles leads to the increase in both r_1 and r_2 values. Therefore, the key factor to obtain T_1 or T_2 dominated CAs is to control the size of MnIO nanoparticles.[26,33] As shown in the SI, Table S1, the r_1 and r_2 relaxivities of iron oxide without Mn doping were 5.85 and 19.70 mM^{-1} s^{-1}, repectively, with lower r_1 value and higher r_2/r_1 ratio than those of MnIO nanoparticles. Therefore, the thus-prepared MnIO nanoparticles with a diameter of 5 nm are effectvie for T_1 positive imaging. When modified with dBSA onto the surface of MnIO nanoparticles, the r_1 value decreased to 3.74 mM^{-1} s^{-1} (SI, Table S1), it can be inferred that the dBSA coating may hinder the interaction between water molecules and metal ions on the surface of MnIO nanoparticles.

In Vitro Photothermal Effect. Theranostic nanoparticles should possess good therapeutic efficacy as well as efficient imaging effect. To evaluate the photothermal effect of the MnIO nanoparticles, their aqueous solutions at different concentrations were exposed to a continuous NIR laser irradiation (808 nm, 2 W) for 5 min. As shown in Figure 4a, the temperature of the MnIO solutions increased rapidly with the increase of exposure time spans and solution concentrations. At concentrations of 125, 250, and 500 μg/mL, the temperature elevations were 18.7, 26.6, and 42.4 °C, respectively. While for pure water, no significant temperature change was observed during 5 min of irradiation. To quantify the photothermal effect, the photothermal conversion efficiency was caculated to be 26.9% (SI, Figure S8), which was comparable to Cu_9S_5 nanocrystals (25.7%)[6] and Au nanorods (21%).[38] The similar photothermal effect of iron oxide based nanomaterials was also observed in other reports.[39,40] The results above demonstrated that the MnIO nanoparticles can be employed as effective photothermal agents.

Inspired by the above experiment, we further explored the feasibility of the MnIO nanoparticles to ablate cancer cells under laser irradiation. 4T1 murine breast cancer cells were incubated with the MnIO-dBSA composites at different concentrations and then exposed to an NIR laser. After 5 min of continuous irradiation, the viability of the cancer cells was measured by standard WST-1 assay. As shown in Figure 4b, single laser irradiation without the assistance of MnIO-dBSA did not result in a noticeable decrease of the cell viability; on the contrary, the presence of the MnIO-dBSA under irradiation significantly induced cell death, which exhibited a dose-dependent profile. More than 80% of the cancer cells were killed at the concentration of 200 μg/mL. Similar phenomena were observed in calcein-AM and PI staining for live (green color) and dead (red color) cell experiment (Figure 4c). The above experiments revealed that the MnIO-dBSA composites play an important role in the heat-induced cancer cell ablation.

In Vivo MR Imaging. On the basis of in vitro T_1 contrast enhancement of the MnIO nanoparticles, we further investigated the in vivo MR imaging performance of the MnIO-dBSA composites. A 4T1 tumor-bearing mouse was injected with 200 μL of MnIO-dBSA solution ([Fe] = 14 mg/kg) through a tail vein. Figure 5a shows T_1-weighted MR images taken before and after injection. Clearly, with the increase of time, gradually enhanced brightness of tumor sites was observed, confirming that the MnIO nanoparticles can increase the T_1 MRI contrast in animal model. To quantify the signal enhancement, we next calculated the signal intensity of the tumor site.[30] Compared with the T_1 signal of preinjection, the T_1 contrast enhancement of the tumor region at 0.5 h p.i. was 1.52 times larger. In the subsequent observation time, the signal enhancement was estimated to be 1.76, 1.88, and 1.91 times at 1, 4, and 6 h p.i., respectively (Figure 5b). The slow increase of signal intensity over time suggested that the accumulation of CAs in the tumor site may be due to the enhanced permeability and retention (EPR) effect.[25] With the circulation of the MnIO-dBSA composites, the signal enhancment gradually decreased and droped to 1.32 times at 12 h p.i. at the tumor site. The in vivo enhanced T_1 positive signal of MnIO-dBSA composites makes them promising CAs to facilitate diagnosis in tumor tissues.

In Vivo Photothermal Therapy. In vivo photothermal therapy of the MnIO-dBSA composites was conducted using 4T1 tumor-bearing mice as animal model. The tumor-bearing mice were intratumorally injected with 100 μL of MnIO-dBSA solution ([Fe] = 40 mg/kg) or the same amount of PBS. The tumor site was irradiated with NIR laser (808 nm, 1.5 W) post 20 min of injection to allow sufficient diffusion of the

DOI: 10.1021/am5080453
ACS Appl. Mater. Interfaces 2015, 7, 4650−4658

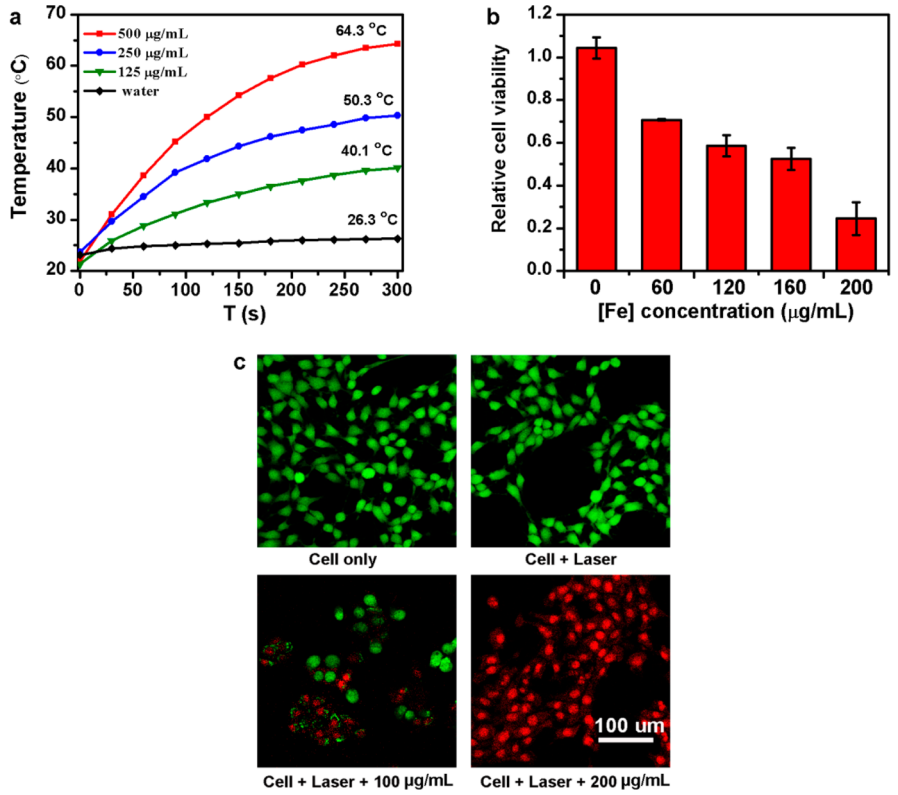

Figure 4. (a) Photothermal effects of water and MnIO solutions at different concentrations ([Fe] = 125, 250, and 500 μg/mL) under laser irradiation (808 nm, 2W) for 5 min. (b) Relative viability of 4T1 cells incubated with MnIO-dBSA at various concentrations ([Fe] = 0, 60, 120, 160, and 200 μg/mL) under laser irradiation (808 nm, 2W) for 5 min. (c) Calceim-AM and PI staining of 4T1 cells. 4T1 cells with no treatment (upper left), with only laser irradiation (upper right), or treated with MnIO-dBSA at Fe concentration of 100 and 200 μg/mL under irradiation for 5 min (bottom).

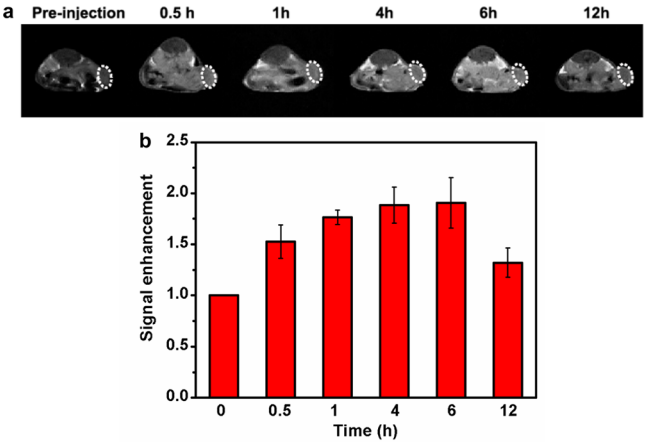

Figure 5. (a) T_1-weighted MR images of a 4T1 tumor-bearing mouse before and after intravenous injection of the MnIO-dBSA solution. The tumor regions were highlighted by white circles. (b) Relative signal enhancement of tumor regions at different time points in the T_1-weighted MR images (n = 3).

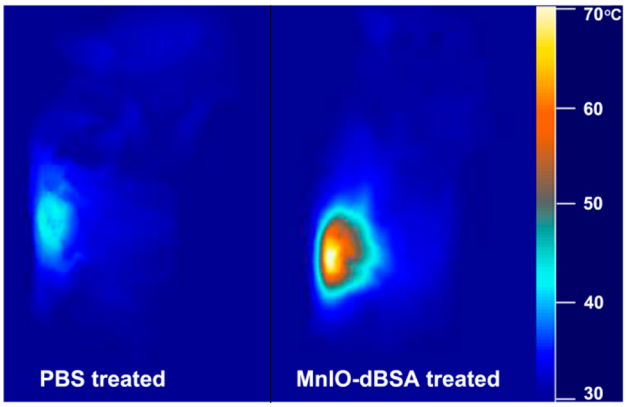

Figure 6. IR thermal images of PBS and MnIO-dBSA treated mice at the end of 5 min laser irradiation.

nanomaterials to the whole tumor region. Figure 6 shows IR thermal images recorded at the end of 5 min irradiation. The surface temperature of the tumor region reached about 70 °C for the MnIO-dBSA treated mice. In contrast, the temperature of the tumor site with PBS injection only rose to 43 °C. The tumor regions for all mice became black after the laser irradiation, and it healed and developed a scab eventually in a week. To evaluate the phtotothermal therapy effect, we monitored the tumor growth in the following 19 days. Due to the efficient hyperthermia treatment, the tumors in MnIO-dBSA with irradiation group were eliminated completely 1 day after laser exposure, and no recurrence of tumors was observed during the next 19 days. For the other three groups, the tumor kept growing, with the tumor size as large as 10−14 fold of the initial tumor size (Figure 7a). Meanwhile, the weight of different groups of mice was also recorded. For all groups, all weight changes maintained in a normal range and no obvious weight loss was observed (Figure 7b).

Histological Assessment. To elucidate the PTT effect to tumor regions, the tumor tissues were collected post 4 h after

DOI: 10.1021/am5080453
ACS Appl. Mater. Interfaces 2015, 7, 4650−4658

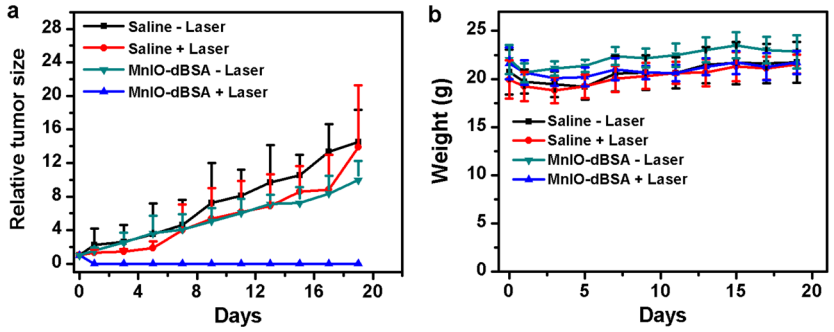

Figure 7. (a) Relative tumor growth curves of different groups of mice in 19 days after various treatments (n = 4 per group). (b) Weight of different groups of mice in 19 days after laser irradiation (n = 4 per group).

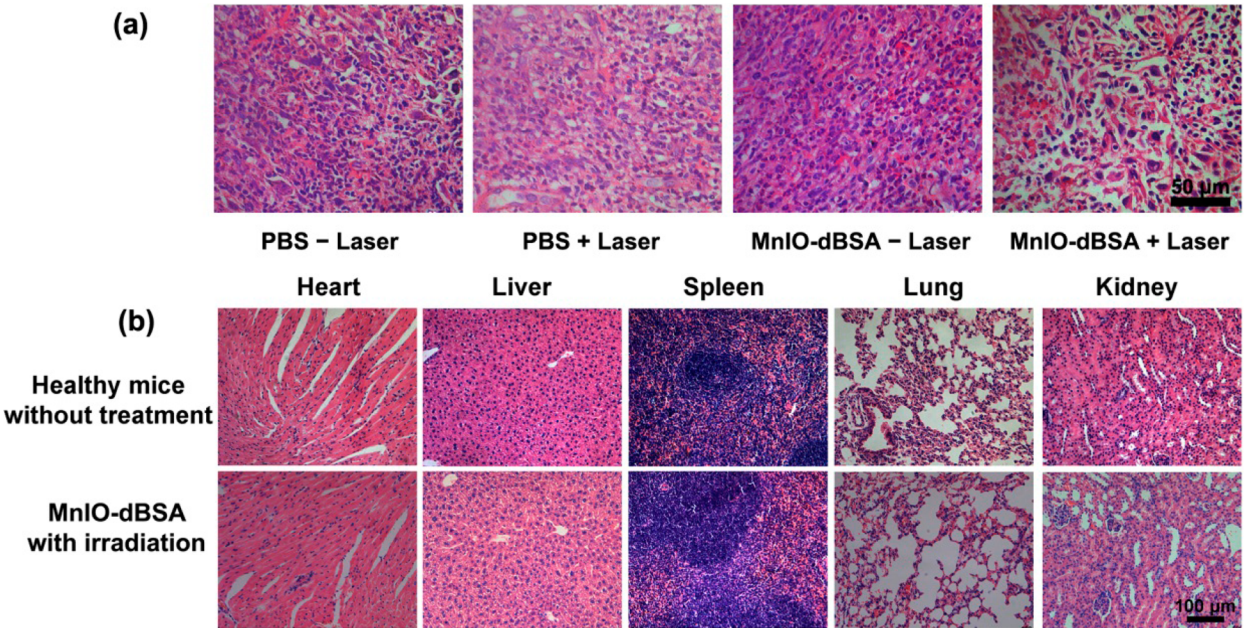

Figure 8. (a) Histological images of H&E stained tumor sections harvested from different groups of mice. (b) H&E staining for major organs (heart, liver, spleen, lung, and kidney). MnIO-dBSA treated mice were sacrificed on the 19th day after laser irradiation. Age-matched healthy mice without treatment were used as a control group (n = 3 per group).

photoirradiation. The histological test revealed the typical cell shrinkage, loss of contact, and nuclear damage in the MnIO-dBSA + laser treated group, which are the major signs of cell damage (Figure 8a). A blood biochemistry analysis was conducted to evaluate the toxicity of MnIO-dBSA composites to the treated mice. The levels of alanine aminotransferase (ALT), aspartate aminotransferase (AST), alkaline phosphatase (ALP), total protein (TP), albumin (ALB), globulin (GLOB), and the ratio of albumin to globulin (A/G) were used to assess the disorders in liver function.[41] Blood urea nitrogen (BUN) and creatinine (CREA) are considered as kidney function markers.[42] No significant abnormality was observed for the MnIO-dBSA treated mice compared with the control group, indicating no obvious damage to the liver and kidney of the mice by MnIO-dBSA treatment (SI, Figure S9). Subsequently, major organs of the mice were harvested for histology analysis. No noticeable pathological changes in major organs were observed by standard hematoxylin and eosin (H&E) stained organ slices (Figure 8b). Though long-term and systematic study is still demanded to completely understand the in vivo toxicity of MnIO-dBSA, our preliminary experiment demonstrated the feasibility of using MnIO-dBSA composites as ideal PTT agents for tumor ablation.

CONCLUSIONS

In summary, we synthesized 5 nm MnIO nanoparticles and then explored their feasibility as T_1 MRI CAs and PTT agents. Our results showed that the thus-prepared MnIO nanoparticles have good positive imaging effect and low r_2/r_1 ratio suitable as T_1 CAs. The in vivo MR imaging experiment using a 4T1 tumor-bearing mouse model exhibited a significant signal enhancement (about two times) at the tumor site. Furthermore, we have demonstrated that hyperthermia caused by the photothermal effect of the MnIO nanoparticles under NIR laser irradiation resulted in significant death of the 4T1 cancer cells. With only one single injection, the MnIO-dBSA composites could efficiently ablate tumor tissues compared to the control groups and showed no obvious recurrence in 19 days. In addition, the blood biochemistry analysis and H&E staining tests suggested the low toxicity of the MnIO-dBSA composites in animal model. Taken all together, this work demonstrated the great potential of MnIO nanoparticles for theranostic applications.

DOI: 10.1021/am5080453
ACS Appl. Mater. Interfaces 2015, 7, 4650−4658

■ ASSOCIATED CONTENT

Supporting Information

XRD pattern, DLS measurements, FT-IR spectra, agarose gel electrophoresis, TGA, stability test, relative cell viability, and blood biochemistry analysis. This material is available free of charge via the Internet at http://pubs.acs.org.

■ AUTHOR INFORMATION

Corresponding Author

*Tel: 86-512-62872556. E-mail: zjzhang2007@sinano.ac.cn.

Notes

The authors declare no competing financial interest.

■ ACKNOWLEDGMENTS

This work was financially supported by National Natural Science Foundation of China (No. 51361130033) and the Ministry of Science and Technology of China (No. 2014CB965003). We thank Prof. Xuefeng Gao and Mr. Jie Zhu for their generous help in providing IR thermal camera.

■ REFERENCES

(1) Shibu, E. S.; Hamada, M.; Murase, N.; Biju, V. Nanomaterials Formulations for Photothermal and Photodynamic Therapy of Cancer. *J. Photochem. Photobiol. C* **2013**, *15*, 53−72.

(2) Cheng, L.; Wang, C.; Feng, L.; Yang, K.; Liu, Z. Functional Nanomaterials for Phototherapies of Cancer. *Chem. Rev.* **2014**, *114*, 10869−10939.

(3) García, D. J.; Maestro, L. M.; del Rosal, B.; Haro, P.; Benayas, A.; Plaza, J. L.; Rodriguez, E. M.; Solé, J. G. Nanoparticles for Photothermal Therapies. *Nanoscale* **2014**, *6*, 9494−9530.

(4) Huang, X.; El-Sayed, I. H.; Qian, W.; El-Sayed, M. A. Cancer Cell Imaging and Photothermal Therapy in the Near-Infrared Region by Using Gold Nanorods. *J. Am. Chem. Soc.* **2006**, *128*, 2115−2120.

(5) Wang, Y.; Black, K. C.; Luehmann, H.; Li, W.; Zhang, Y.; Cai, X.; Wan, D.; Liu, S. Y.; Li, M.; Kim, P. Comparison Study of Gold Nanohexapods, Nanorods, and Nanocages for Photothermal Cancer Treatment. *ACS Nano* **2013**, *7*, 2068−2077.

(6) Tian, Q.; Jiang, F.; Zou, R.; Liu, Q.; Chen, Z.; Zhu, M.; Yang, S.; Wang, J.; Wang, J.; Hu, J. Hydrophilic Cu_9S_5 Nanocrystals: A Photothermal Agent With a 25.7% Heat Conversion Efficiency for Photothermal Ablation of Cancer Cells In Vivo. *ACS Nano* **2011**, *5*, 9761−9771.

(7) Liu, T.; Wang, C.; Gu, X.; Gong, H.; Cheng, L.; Shi, X.; Feng, L.; Sun, B.; Liu, Z. Drug Delivery with PEGylated MoS_2 Nano-Sheets for Combined Photothermal and Chemotherapy of Cancer. *Adv. Mater.* **2014**, *26*, 3433−3440.

(8) Chou, S. S.; Kaehr, B.; Kim, J.; Foley, B. M.; De, M.; Hopkins, P. E.; Huang, J.; Brinker, C. J.; Dravid, V. P. Chemically Exfoliated MoS_2 as Near-Infrared Photothermal Agents. *Angew. Chem., Int. Ed.* **2013**, *125*, 4254−4258.

(9) Kam, N. W. S.; O'Connell, M.; Wisdom, J. A.; Dai, H. Carbon Nanotubes as Multifunctional Biological Transporters and Near-Infrared Agents for Selective Cancer Cell Destruction. *Proc. Natl. Acad. Sci. U.S.A.* **2005**, *102*, 11600−11605.

(10) Singh, R.; Torti, S. V. Carbon Nanotubes in Hyperthermia Therapy. *Adv. Drug Delivery Rev.* **2013**, *65*, 2045−2060.

(11) Tu, X.; Ma, Y.; Cao, Y.; Huang, J.; Zhang, M.; Zhang, Z. PEGylated Carbon Nanoparticles for Efficient In Vitro Photothermal Cancer Therapy. *J. Mater. Chem. B* **2014**, *2*, 2184−2192.

(12) Chu, M.; Peng, J.; Zhao, J.; Liang, S.; Shao, Y.; Wu, Q. Laser Light Triggered-Activated Carbon Nanosystem for Cancer Therapy. *Biomaterials* **2013**, *34*, 1820−1832.

(13) Yang, K.; Zhang, S.; Zhang, G.; Sun, X.; Lee, S. T.; Liu, Z. Graphene in Mice: Ultrahigh In Vivo Tumor Uptake and Efficient Photothermal Therapy. *Nano Lett.* **2010**, *10*, 3318−3323.

(14) Robinson, J. T.; Tabakman, S. M.; Liang, Y.; Wang, H.; Sanchez Casalongue, H.; Vinh, D.; Dai, H. Ultrasmall Reduced Graphene Oxide with High Near-Infrared Absorbance for Photothermal Therapy. *J. Am. Chem. Soc.* **2011**, *133*, 6825−6831.

(15) Kelkar, S. S.; Reineke, T. M. Theranostics: Combining Imaging and Therapy. *Bioconjugate Chem.* **2011**, *22*, 1879−1903.

(16) Xu, W.; Kattel, K.; Park, J. Y.; Chang, Y.; Kim, T. J.; Lee, G. H. Paramagnetic Nanoparticle T_1 and T_2 MRI Contrast Agents. *Phys. Chem. Chem. Phys.* **2012**, *14*, 12687−12700.

(17) Lam, T.; Pouliot, P.; Avti, P. K.; Lesage, F.; Kakkar, A. K. Superparamagnetic Iron Oxide Based Nanoprobes for Imaging and Theranostics. *Adv. Colloid Interface Sci.* **2013**, *199*−*200*, 95−113.

(18) Kim, B. H.; Lee, N.; Kim, H.; An, K.; Park, Y. I.; Choi, Y.; Shin, K.; Lee, Y.; Kwon, S. G.; Na, H. B. Large-Scale Synthesis of Uniform and Extremely Small-Sized Iron Oxide Nanoparticles for High-Resolution T_1 Magnetic Resonance Imaging Contrast Agents. *J. Am. Chem. Soc.* **2011**, *133*, 12624−12631.

(19) Hao, R.; Xing, R.; Xu, Z.; Hou, Y.; Gao, S.; Sun, S. Synthesis, Functionalization, and Biomedical Applications of Multifunctional Magnetic Nanoparticles. *Adv. Mater.* **2010**, *22*, 2729−2742.

(20) Yoo, D.; Lee, J. H.; Shin, T. H.; Cheon, J. Theranostic Magnetic Nanoparticles. *Acc. Chem. Res.* **2011**, *44*, 863−874.

(21) Lee, S. H.; Kim, B. H.; Na, H. B.; Hyeon, T. Paramagnetic Inorganic Nanoparticles as T_1 MRI Contrast Agents. *Wiley Interdiscip. Rev.: Nanomed. Nanobiotechnol.* **2014**, *6*, 196−209.

(22) Tan, M.; Ye, Z.; Jeong, E. K.; Wu, X.; Parker, D. L.; Lu, Z. R. Synthesis and Evaluation of Nanoglobular Macrocyclic Mn(II) Chelate Conjugates as Non-Gadolinium (III) MRI Contrast Agents. *Bioconjugate Chem.* **2011**, *22*, 931−937.

(23) Kucheryavy, P.; He, J.; John, V. T.; Maharjan, P.; Spinu, L.; Goloverda, G. Z.; Kolesnichenko, V. L. Superparamagnetic Iron Oxide Nanoparticles with Variable Size and an Iron Oxidation State as Prospective Imaging Agents. *Langmuir* **2013**, *29*, 710−716.

(24) Jun, Y. W.; Seo, J. W.; Cheon, J. Nanoscaling Laws of Magnetic Nanoparticles and Their Applicabilities in Biomedical Sciences. *Acc. Chem. Res.* **2008**, *41*, 179−189.

(25) Zhou, Z.; Wang, L.; Chi, X.; Bao, J.; Yang, L.; Zhao, W.; Chen, Z.; Wang, X.; Chen, X.; Gao, J. Engineered Iron-Oxide-Based Nanoparticles as Enhanced T_1 Contrast Agents for Efficient Tumor Imaging. *ACS Nano* **2013**, *7*, 3287−3296.

(26) Li, Z.; Wang, S. X.; Sun, Q.; Zhao, H. L.; Lei, H.; Lan, M. B.; Cheng, Z. X.; Wang, X. L.; Dou, S. X. Ultrasmall Manganese Ferrite Nanoparticles as Positive Contrast Agent for Magnetic Resonance Imaging. *Adv. Healthcare Mater.* **2013**, *2*, 958−964.

(27) Zeng, L.; Ren, W.; Zheng, J.; Cui, P.; Wu, A. Ultrasmall Water-Soluble Metal-Iron Oxide Nanoparticles as T_1-Weighted Contrast Agents for Magnetic Resonance Imaging. *Phys. Chem. Chem. Phys.* **2012**, *14*, 2631−2636.

(28) Shen, L. H.; Bao, J. F.; Wang, D.; Wang, Y. X.; Chen, Z. W.; Ren, L.; Zhou, X.; Ke, X. B.; Chen, M.; Yang, A. Q. One-Step Synthesis of Monodisperse, Water-Soluble Ultra-Small Fe_3O_4 Nanoparticles for Potential Bio-Application. *Nanoscale* **2013**, *5*, 2133−2141.

(29) Gao, X.; Chan, W. C.; Nie, S. Quantum-Dot Nanocrystals for Ultrasensitive Biological Labeling and Multicolor Optical Encoding. *J. Biomed. Opt.* **2002**, *7*, 532−537.

(30) Lee, J. H.; Huh, Y. M.; Jun, Y. W.; Seo, J. W.; Jang, J. T.; Song, H. T.; Kim, S.; Cho, E. J.; Yoon, H. G.; Suh, J. S. Artificially Engineered Magnetic Nanoparticles for Ultra-Sensitive Molecular Imaging. *Nat. Med.* **2006**, *13*, 95−99.

(31) Liu, Y.; Ai, K.; Liu, J.; Deng, M.; He, Y.; Lu, L. Dopamine-Melanin Colloidal Nanospheres: An Efficient Near-Infrared Photothermal Therapeutic Agent for In Vivo Cancer Therapy. *Adv. Mater.* **2013**, *25*, 1353−1359.

(32) Huang, J.; Wang, L.; Zhong, X.; Li, Y.; Yang, L.; Mao, H. Facile Non-Hydrothermal Synthesis of Oligosaccharide Coated Sub-5 nm Magnetic Iron Oxide Nanoparticles with Dual MRI Contrast Enhancement Effects. *J. Mater. Chem. B* **2014**, *2*, 5344−5351.

(33) Huang, G.; Li, H.; Chen, J.; Zhao, Z.; Yang, L.; Chi, X.; Chen, Z.; Wang, X.; Gao, J. Tunable T_1 and T_2 Contrast Abilities of

DOI: 10.1021/am5080453
ACS Appl. Mater. Interfaces 2015, 7, 4650−4658

Manganese-Engineered Iron Oxide Nanoparticles through Size Control. *Nanoscale* **2014**, *6*, 10404−10412.
(34) Wang, Q.; Kuo, Y.; Wang, Y.; Shin, G.; Ruengruglikit, C.; Huang, Q. Luminescent Properties of Water-Soluble Denatured Bovine Serum Albumin-Coated CdTe Quantum Dots. *J. Phys. Chem. B* **2006**, *110*, 16860−16866.
(35) Zhang, L.; Lu, Z.; Bai, Y.; Wang, T.; Wang, Z.; Chen, J.; Ding, Y.; Yang, F.; Xiao, Z.; Ju, S. PEGylated Denatured Bovine Serum Albumin Modified Water-Soluble Inorganic Nanocrystals as Multifunctional Drug Delivery Platforms. *J. Mater. Chem. B* **2013**, *1*, 1289−1295.
(36) Hlavacek, A.; Bouchal, P.; Skládal, P. Biotinylation of Quantum Dots for Application in Fluoroimmunoassays with Biotin-Avidin Amplification. *Microchim. Acta* **2012**, *176*, 287−293.
(37) Park, J. Y.; Baek, M. J.; Choi, E. S.; Woo, S.; Kim, J. H.; Kim, T. J.; Jung, J. C.; Chae, K. S.; Chang, Y.; Lee, G. H. Paramagnetic Ultrasmall Gadolinium Oxide Nanoparticles as Advanced T_1 MRI Contrast Agent: Account for Large Longitudinal Relaxivity, Optimal Particle Diameter, and In Vivo T_1 MR Images. *ACS Nano* **2009**, *3*, 3663−3669.
(38) Hessel, C. M.; P. Pattani, V.; Rasch, M.; Panthani, M. G.; Koo, B.; Tunnell, J. W.; Korgel, B. A. Copper Selenide Nanocrystals for Photothermal Therapy. *Nano Lett.* **2011**, *11*, 2560−2566.
(39) Chu, M.; Shao, Y.; Peng, J.; Dai, X.; Li, H.; Wu, Q.; Shi, D. Near-Infrared Laser Light Mediated Cancer Therapy by Photothermal Effect of Fe_3O_4 Magnetic Nanoparticles. *Biomaterials* **2013**, *34*, 4078−4088.
(40) Zhou, Z.; Sun, Y.; Shen, J.; Wei, J.; Yu, C.; Kong, B.; Liu, W.; Yang, H.; Yang, S.; Wang, W. Iron/Iron Oxide Core/Shell Nanoparticles for Magnetic Targeting MRI and Near-Infrared Photothermal Therapy. *Biomaterials* **2014**, *35*, 7470−7478.
(41) Zhang, Z.; Wang, J.; Nie, X.; Wen, T.; Ji, Y.; Wu, X.; Zhao, Y.; Chen, C. Near Infrared Laser Induced Targeted Cancer Therapy Using Thermo-Responsive Polymer Encapsulated Gold Nanorods. *J. Am. Chem. Soc.* **2014**, *136*, 7317−7326.
(42) Yang, K.; Xu, H.; Cheng, L.; Sun, C.; Wang, J.; Liu, Z. In Vitro and In Vivo Near-Infrared Photothermal Therapy of Cancer Using Polypyrrole Organic Nanoparticles. *Adv. Mater.* **2012**, *24*, 5586−5592.

DOI: 10.1021/am5080453
ACS Appl. Mater. Interfaces 2015, 7, 4650−4658